

Research Paper

Circular RNA SCMHI suppresses KMO expression to inhibit mitophagy and promote functional recovery following stroke

Yu Wang¹, Ying Bai¹, Yang Cai¹, Yuan Zhang¹, Ling Shen¹, Wen Xi¹, Zhongqiu Zhou¹, Lian Xu¹, Xue Liu¹, Bing Han¹, Honghong Yao^{1,2,3}

1. Jiangsu Provincial Key Laboratory of Critical Care Medicine, Department of Pharmacology, School of Medicine, Southeast University, Nanjing, China.
2. Co-innovation Center of Neuroregeneration, Nantong University, Nantong, China.
3. Institute of Life Sciences, Key Laboratory of Developmental Genes and Human Disease, Southeast University, Nanjing, China.

 Corresponding authors: Honghong Yao, Ph.D., Jiangsu Provincial Key Laboratory of Critical Care Medicine, Department of Pharmacology, School of Medicine, Southeast University, Nanjing, China; Tel: +8625 83272551; E-mail: yaohh@seu.edu.cn; Bing Han, Ph.D., Jiangsu Provincial Key Laboratory of Critical Care Medicine, Department of Pharmacology, School of Medicine, Southeast University, Nanjing, China; Tel: +8625 83272551; E-mail: hanb@seu.edu.cn.

© The author(s). This is an open access article distributed under the terms of the Creative Commons Attribution License (<https://creativecommons.org/licenses/by/4.0/>). See <https://ivyspring.com/terms> for full terms and conditions.

Received: 2024.06.06; Accepted: 2024.09.29; Published: 2024.10.28

Abstract

Rationale: Metabolic dysfunction is one of the key pathological events after ischemic stroke. Disruption of cerebral blood flow impairs oxygen and energy substrate delivery, leading to mitochondrial oxidative phosphorylation dysfunction and cellular bioenergetic stress. Investigating the effects of circSCMHI, a brain repair-related circular RNA, on metabolism may identify novel therapeutic targets for stroke treatment.

Methods: CircSCMHI was encapsulated into brain-targeting extracellular vesicles (EVs) mediated by rabies virus glycoprotein (RVG). Using a mouse model of photothrombotic (PT) stroke, we employed metabolomics and transcriptomics, combined with western blotting and behavioral experiments, to identify the metabolic targets regulated in RVG-circSCMHI-EV-treated mice. Additionally, immunofluorescence staining, chromatin immunoprecipitation (ChIP), pull-down, and western blotting were utilized to elucidate the underlying mechanisms.

Results: The targeted delivery of circSCMHI via RVG-EVs was found to promote post-stroke brain repair by enhancing mitochondrial fusion and inhibiting mitophagy through suppression of kynurenine 3-monooxygenase (KMO) expression. Mechanistically, circSCMHI exerted its inhibitory effect on KMO expression by binding to the transcription activator STAT5B, thereby impeding its nuclear translocation.

Conclusions: Our study reveals a novel mechanism by which circSCMHI downregulates KMO expression, thereby enhancing mitochondrial fusion and inhibiting mitophagy, ultimately facilitating post-stroke brain repair. These findings shed new light on the role of circSCMHI in promoting stroke recovery and underscore its potential as a therapeutic target for the treatment of ischemic stroke.

Keywords: circSCMHI, functional recovery, ischemic stroke, KMO, STAT5B

Introduction

Ischemic stroke is a leading cause of adult disability, characterized by neurological deficits caused by cerebrovascular occlusion [1-3]. At present, therapeutic agents to promote stroke recovery and improve long-term outcomes are lacking [4]. High levels of oxygen and glucose are essential for the brain, due to its high intrinsic metabolic activity [5].

Growing evidence demonstrates that metabolic reprogramming after stroke improves long-term neurological function and is strongly associated with high survival rates in animal models and stroke patients [6, 7]. Efforts to explore therapeutic approaches to promoting post-stroke metabolic reprogramming are vital areas of research that have

provided benefits to many ischemic stroke patients.

Among various molecules, circular RNAs (circRNAs) have garnered increasing attention in recent years for their role in regulating various metabolic pathways, such as glucose, lipid, and amino acid metabolism [8-10]. As one type of endogenous non-coding RNA molecules, circRNAs are characterized by their covalently closed continuous loops formed through back-splicing [11-13]. Previous studies have shown that circRNAs are widely distributed in the brain, and several of them, such as circHECTD1, circDLGAP4, circTLK1, circFoxO3, and circSCMH1, have been functionally linked to ischemic stroke [14-18]. This revealed that developing therapeutic drugs targeting circRNAs was a viable direction for the treatment of ischemic stroke.

In our previous study, we discovered that circSCMH1 was expressed in various cell types in the brain and promoted post-stroke brain repair by enhancing neuronal plasticity and facilitating vascular repair [18, 19]. To increase the clinical translational value of circSCMH1 research, we utilized extracellular vesicles (EVs), which are a heterogeneous collection of lipid bilayer-enclosed particles released from cells and have the ability to cross the blood-brain barrier (BBB) to deliver functional cargoes to recipient cells [20-22]. By incorporating acetylcholine receptor (AChR)-specific rabies virus glycoprotein (RVG) peptides, the EVs were enabled to specifically deliver circSCMH1 to various cell types in the brain [18, 23]. Additionally, our previous study indicated that these RVG-circSCMH1-EVs effectively promoted brain repair post-stroke in rhesus monkeys, highlighting their substantial clinical applicability. However, the role of metabolism in the regulatory process of circSCMH1 on brain repair post-stroke remains unknown.

This study investigates the metabolism in the context of circSCMH1-mediated functional recovery following stroke. Our data demonstrated that inhibiting kynurenine 3-monooxygenase (KMO), a metabolic enzyme involved in the kynurenine pathway (KP), improved mitochondrial dynamics and inhibited mitophagy after stroke [24]. We further elucidated the specific mechanism by which KMO regulates functional recovery following stroke, underscoring a novel mitochondrial role for KMO. This effect was independent of KMO enzymatic activity, as circSCMH1 did not reduce the 3-hydroxykynurenine (3-HK) concentration in photothrombotic (PT) stroke mice. Mechanically, circSCMH1 bound to STAT5B and inhibited its nuclear translocation, leading to a decrease in KMO

expression. Our findings thus revealed that circSCMH1 was able to enhance functional recovery via KMO-regulated mitophagy, providing a previously overlooked mechanism through which circSCMH1 promotes stroke recovery.

Results

CircSCMH1 regulates metabolic disorders and inhibits KMO expression after cerebral ischemia

Metabolomic analyses were performed on the peri-infarcted cortex of PT mice treated with circSCMH1 on day 3 after stroke. These results revealed significant changes in the metabolomic profile of PT mice compared with sham mice after ischemic stroke, as indicated by principal component analysis (PCA) (Figure 1A). We identified 346 metabolites that changed significantly in PT mice after circSCMH1 treatment that were altered by at least $[\log_2(\text{fold change})] \geq 1$ with a P -value < 0.05 (Figure 1B). These significantly altered metabolites were correlated with circSCMH1, and most were associated with amino acids and the amino acid metabolic pathways, as identified using Metaboanalyst (Figure S1A-B). To explore the mechanisms underlying the observed changes in metabolic processes after cerebral ischemia, transcriptomic analyses were performed using samples from the peri-infarcted cortex of PT mice on day 3 post-stroke. A total of 148 genes associated with circSCMH1 were screened (Figure S1C), and subsequent metabolic pathway enrichment analyses revealed a notable enrichment in pathways related to amino acid metabolism (Figure 1C).

Through the integration of RNA-seq and metabolomics data, pathways altered in response to circSCMH1 after PT treatment were identified (Figure 1D), unveiling 14 genes related to metabolism (Figure 1E). As both transcriptomic and metabolomic pathway enrichment analyses revealed the most significant enrichment in amino acid metabolic pathways, four genes (*Th*, *Prdm6*, *Kmo*, and *Aoc3*) that were involved in five amino acid metabolic pathways were screened out (Figure 1F-G). Of these, only *Kmo*, encoding a key enzyme in the KP, exhibited an expression trend that was validated (Figure S1D). RVG-circSCMH1-EVs treatment significantly decreased inducible KMO expression in the peri-infarct cortex of PT mice, as confirmed by western blotting (Figure 1H-I). Taken together, our analyses indicated that circSCMH1 regulated the KP after ischemic stroke by inhibiting the expression of KMO.

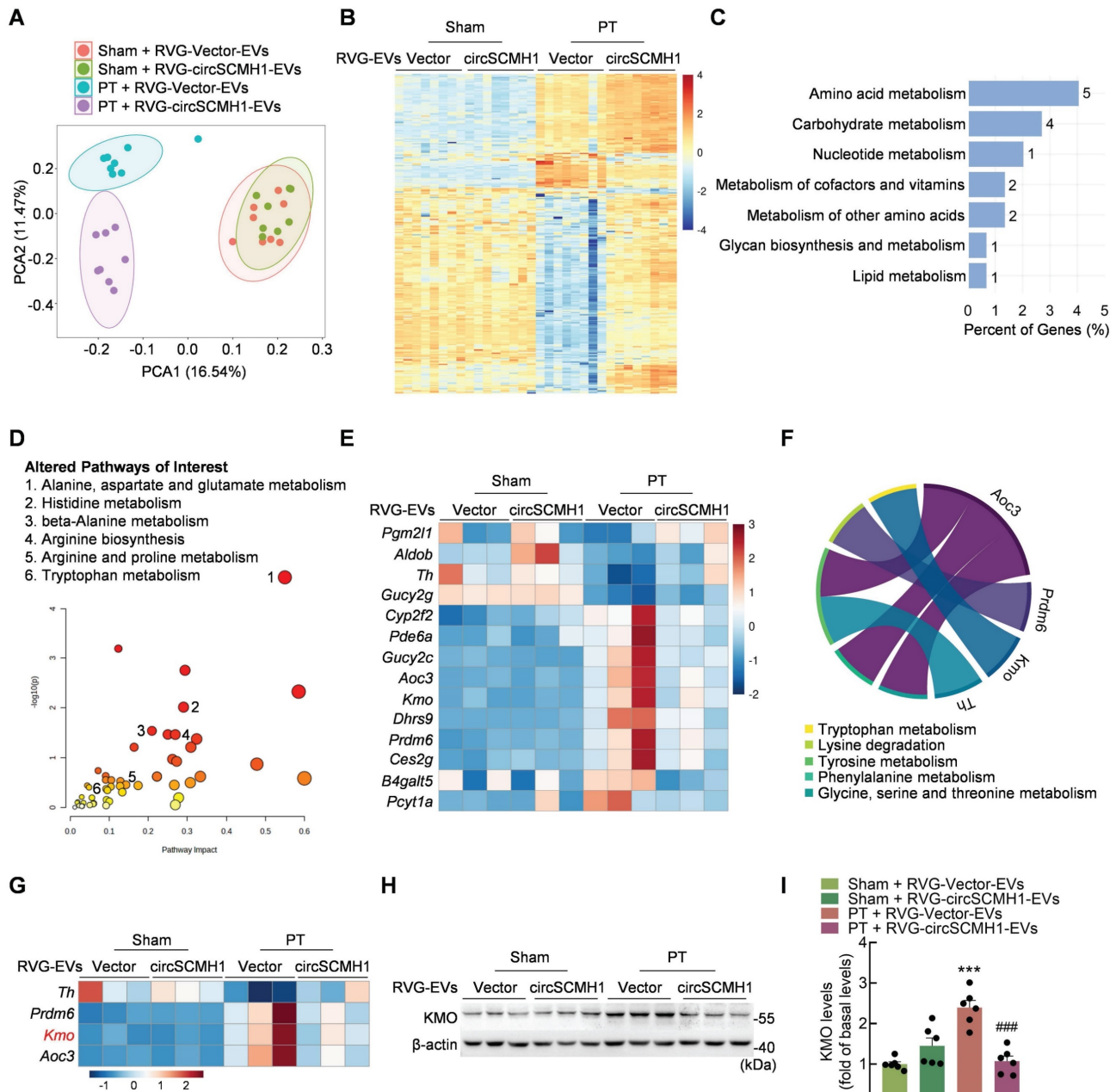


Figure 1. CircSCMH1 regulates metabolic disorders and inhibits KMO expression after cerebral ischemia. (A) Principal component analysis (PCA) of the metabolome in PT and sham mice overexpressing circSCMH1 or Vector (n = 8). Each symbol represents the data for an individual mouse. (B) Heatmap analysis of 346 differential metabolites in PT and sham mice overexpressing circSCMH1 or Vector (n = 8). (C) Metabolism-related KEGG pathway enrichment analysis of 148 differentially expressed genes ($[\log_2(\text{fold change})] \geq 1$ and $P\text{-value} < 0.05$). (D) Pathways altered in PT mice treated with circSCMH1 identified based on transcriptomic and metabolomics data. Metabolic pathways of interest are highlighted. (E) Heatmap analysis of 14 genes involved in metabolism identified in transcriptomic analyses (n = 3). (F) Chord diagrams visualizing the interrelationships between amino acids metabolism-related genes and amino acids metabolic pathways. (G) Heatmap analysis of 4 genes involved in amino acid metabolism identified in transcriptomic analyses (n = 3). (H, I) Western blotting analysis of post-stroke KMO expression in mice. Three representative immunoblots are presented from 6 mice/group. $***P < 0.001$ versus the sham + RVG-Vector-EVs group; $###P < 0.001$ versus the PT + RVG-Vector-EVs group using 2-way ANOVA followed by Holm-Sidak post hoc multiple comparisons test. CircSCMH1, circular RNA SCMH1; EVs, extracellular vesicles; KMO, kynurenine 3-monooxygenase; PCA, principal component analysis; PT, photothrombotic stroke; RVG, rabies virus glycoprotein.

The reparative post-stroke function of circSCMH1 is independent of KMO enzymatic activity

In addition to the observed impact of circSCMH1 on KMO expression, metabolomics analyses revealed that the concentration of tryptophan (Trp) was affected by circSCMH1 treatment. To investigate the

effects of circSCMH1 on metabolites involved in the KP, targeted metabolomics analyses were conducted revealing that Trp, kynurenine (Kyn), and 3-HK concentrations increased significantly in the peri-infracted cortex of PT mice. Surprisingly, Trp and Kyn levels decreased significantly following circSCMH1 treatment, while 3-HK levels exhibited a decreasing trend (Figure 2A-B). This result

demonstrated that the effect of circSCMH1 on post-stroke functional recovery was independent of the enzymatic activity of KMO, suggesting that they instead act through a novel mechanism. Thus, we hypothesized that circSCMH1 facilitates functional recovery by regulating the expression of KMO.

KMO inhibition enhances functional recovery after ischemic stroke

To explore the impact of KMO on the functional recovery of PT mice and to determine whether its effect was regulated by circSCMH1, we overexpressed KMO by microinjecting either the Vector-GFP or KMO-GFP lentivirus (LV) into the contralateral lateral ventricle of mice two weeks before PT surgery. The level of KMO expression was elevated in ipsilateral cortex after KMO-GFP lentivirus microinjecting (Figure S2A-C). Pretrained male mice were subjected to PT followed by intravenous administration of RVG-Vector/circSCMH1-EVs at 24 h after surgery. Behavioral testing was performed from days 3 to 28 after PT stroke (Figure 3A). Treatment with RVG-circSCMH1-EVs at 24 h after stroke promoted motor recovery [18]. As shown in behavioral tests, in comparison to the LV-Vector group, animals administered LV-KMO exhibited impaired performance after treatment with RVG-circSCMH1-EVs, as evidenced by increased foot faults on days 3, 7, 14, 21, and 28 following PT surgery (Figure 3B). In the cylinder test, mice treated with LV-KMO showed significantly increased bias at days 3, 7, 14, 21 and 28 after PT model induction (Figure 3C). Furthermore, significant damage-related effects were observed in the adhesive removal test, reflected by the increased removal time after LV-KMO treatment compared with the LV-Vector on days 4, 7, 14, 21, and 28 after PT model induction (Figure 3D). In contrast, LV-Vector treatment did not affect the therapeutic effect of circSCMH1. Collectively, these results demonstrated that circSCMH1 promoted motor recovery by inhibiting the expression of KMO.

KMO inhibition after circSCMH1 treatment in PT mice regulates mitochondria dynamics

The overexpression of human KMO in mammalian cells in a prior study revealed that KMO is involved in the post-translational regulation of DRP1, suggesting that KMO plays a role in mitochondrial dynamics and mitophagy, independent of its enzymatic function in the KP [25]. To investigate the effect of circSCMH1 on mitochondrial dynamics through the regulation of KMO expression, its impact on mitochondrial dynamics was examined in PT mice. Treatment with RVG-circSCMH1-EVs significantly increased the levels of OPA1 and MFN2 in the

peri-infarct cortex of PT mice, although there was no significant difference in the expression of DRP1 (Figure 4A-C). Meanwhile, KMO overexpression eliminated the increased expression of OPA1 and MFN2 but had no effect on DRP1 expression (Figure 4D-F). Immunofluorescence staining was also used to confirm the effect of circSCMH1 treatment on mitochondrial morphology. This approach revealed that mitochondria exhibited a long tubular shape in sham mice, whereas the mitochondrial network was almost completely fragmented in PT mice. Interestingly, treatment with circSCMH1 significantly inhibited the morphological transition of mitochondria, and this inhibitory effect was abolished by KMO overexpression (Figure 4G). The results showed that mitochondrial dynamics were affected by circSCMH1 through the inhibition of KMO expression.

CircSCMH1 inhibits mitophagy via suppressing post-stroke KMO expression

Mitochondrial fusion/fission induce mitophagy [26]. In order to explore the effect of circSCMH1 on mitophagy, the levels of proteins that associated with mitophagy activation were examined. We found that circSCMH1 treatment led to a decrease in the expression of LC3B (microtubule-associated protein 1 light chain 3 beta)-II, a general autophagosomal marker, in PT mice (Figure 5A), indicating that circSCMH1 prevented the formation of autophagosomes. This conclusion was supported by the results of SQSTM1 (sequestosome 1; a receptor protein that links LC3B with ubiquitin) immunoblotting performed on PT mice after circSCMH1 therapy (Figure 5B). Furthermore, the levels of the mitochondrial proteins TOM20 and COX4I1, which are indicators of mitochondrial content, decreased in the brains of PT-treated mice, while circSCMH1 treatment attenuated the decrease in these proteins (Figure 5C-D).

Next, we investigated whether circSCMH1 was able to affect mitophagy by regulating the expression of KMO. The PT mice overexpressing KMO exhibited a dramatic reversal of the elevated levels of the mitochondrial marker proteins (TOM20 and COX4I1), together with the elevation of LC3B-II and a reduction in the autophagy substrate SQSTM1 in response to circSCMH1 therapy (Figure 5E-H). These results indicated that KMO alleviated the inhibitory effect of circSCMH1 on mitophagy. To further confirm the effect of circSCMH1 on mitophagy, co-staining for LC3B and TOM20 was performed. In the peri-infarct cortex of PT mice, the notable co-localization of TOM20 and LC3B was observed, indicative of an increased level of mitophagy. Notably, treatment with

circSCMH1 resulted in a reduction in their co-localization, suggesting an inhibitory effect of circSCMH1 on mitophagy. Additionally, the overexpression of KMO led to an increase in the co-localization of TOM20 and LC3B, implicating KMO

in the regulation of mitophagy (Figure 5I). These results supported the conclusion that circSCMH1 inhibited mitophagy by suppressing KMO expression after PT treatment.

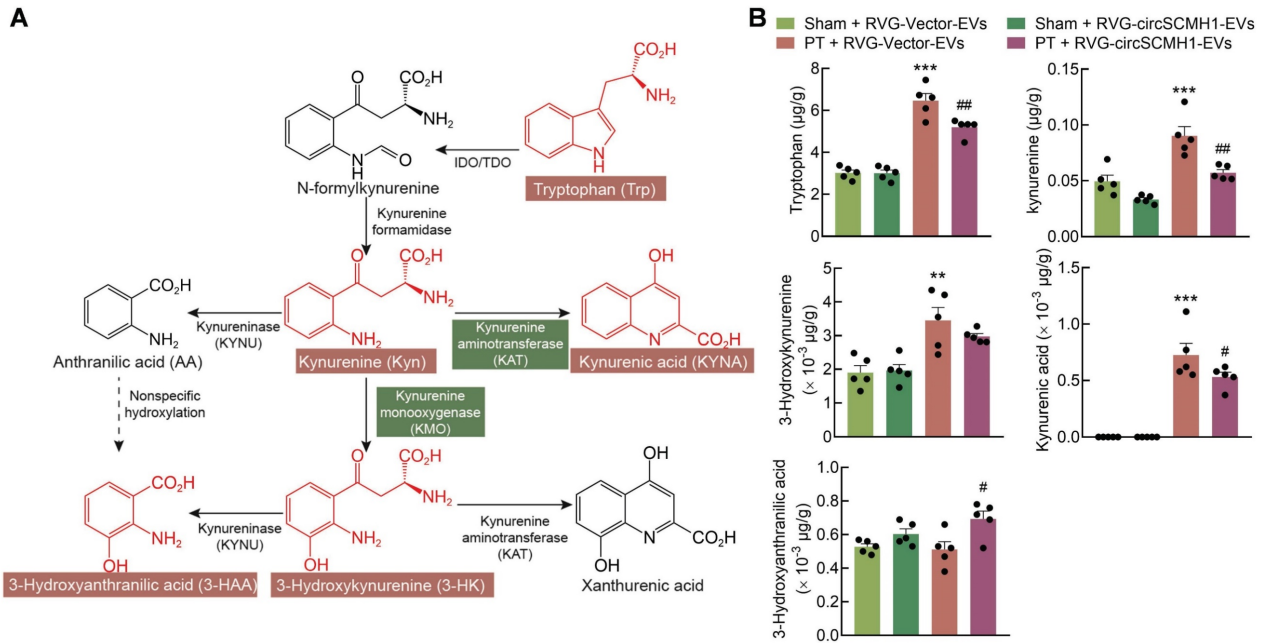


Figure 2. The reparative post-stroke function of circSCMH1 is independent of KMO enzymatic activity. (A) Diagram of the kynurenine pathway. (B) CircSCMH1-treated mouse steady-state kynurenine metabolite tissue concentrations of tryptophan, kynurenine, 3-hydroxykynurenine, kynurenic acid, and 3-hydroxyanthranilic acid. n = 5 animals/group. **P < 0.01, ***P < 0.001 versus Sham + RVG-Vector-EVs group; #P < 0.05, ###P < 0.01 versus PT + RVG-Vector-EVs group using 2-way ANOVA followed by Holm-Sidak post hoc multiple comparisons test. EVs, extracellular vesicles; KMO, kynurenine 3-monooxygenase; PT, photothrombotic stroke; RVG, rabies virus glycoprotein.

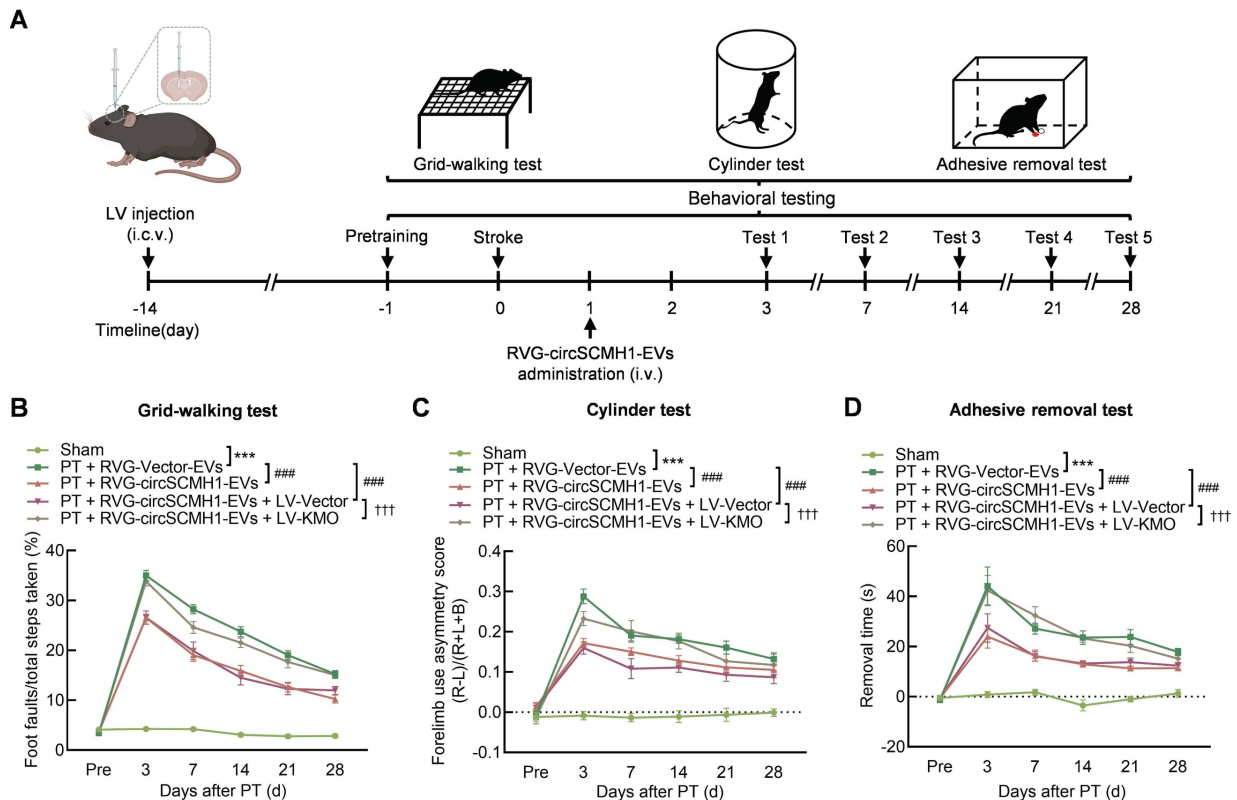


Figure 3. KMO inhibition enhances functional recovery after ischemic stroke. (A) Schematic overview of LV-KMO, RVG-circSCMH1-EVs administration, and behavioral studies. (B-D) KMO eliminated the beneficial effect of circSCMH1 on behavioral recovery at different time points after stroke as measured by the grid-walking test,

cylinder test, and adhesive removal test; L indicates left forepaw in the cylinder test; R, right forepaw in the cylinder test; B, both forepaws in the cylinder test. n = 15 animals/group. ****P* < 0.001 versus the sham group; ####*P* < 0.001 versus the PT + RVG-Vector-EVs group; †††*P* < 0.001 versus the PT + RVG-circSCMH1-EVs + LV-Vector group using 2-way ANOVA followed by Holm-Sidak post hoc multiple comparisons test. EVs, extracellular vesicles; i.c.v., intracerebroventricular injection; i.v., intravenous injection; KMO, kynurenine 3-monooxygenase; LV, lentivirus; PT, phot thrombotic stroke; RVG, rabies virus glycoprotein.

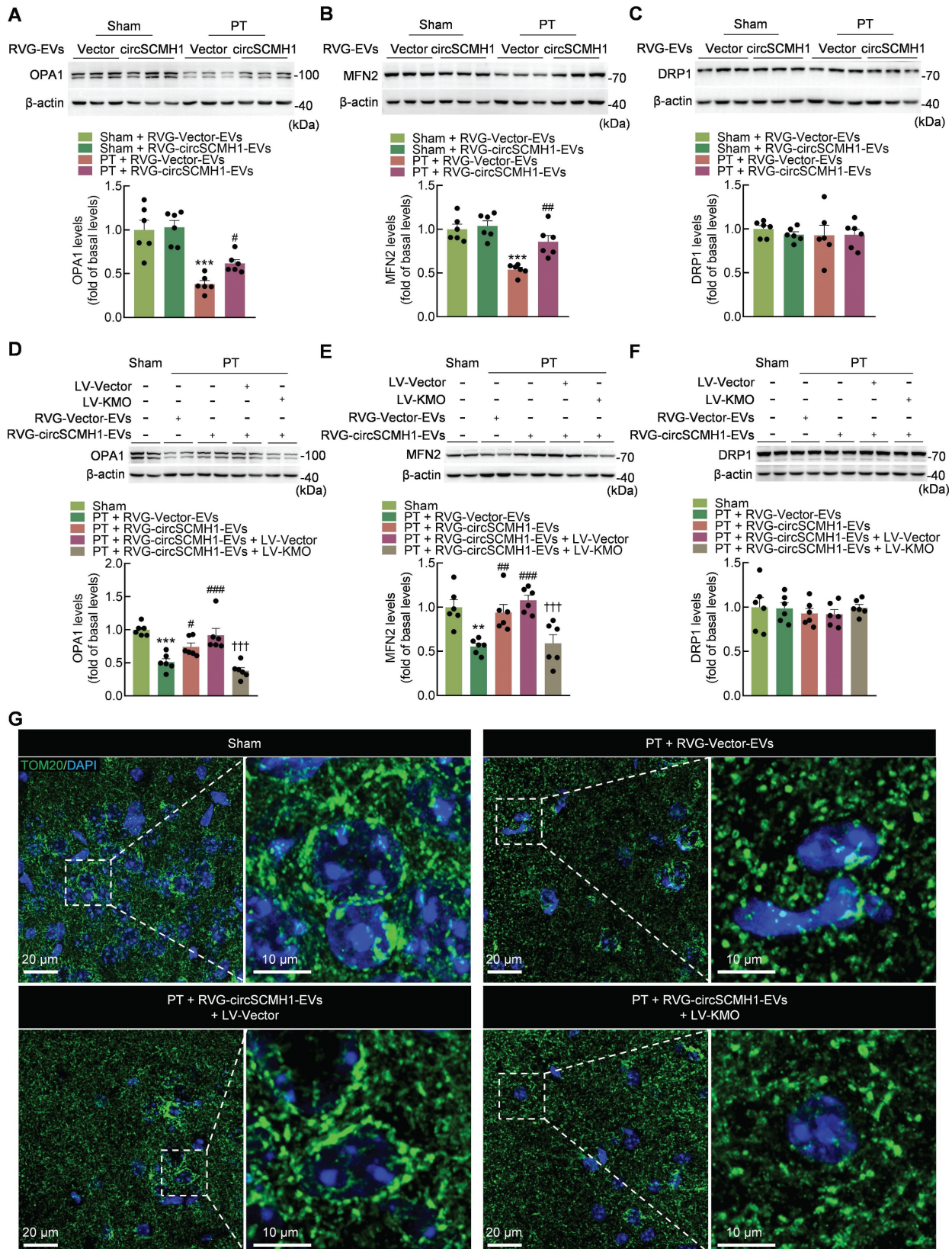


Figure 4. KMO inhibition after circSCMH1 treatment in PT mice regulates mitochondria dynamics. (A-C) Effect of RVG-circSCMH1-EVs on OPA1, MFN2 and DRP1 levels in mice on day 3 after PT (n = 6 for each group). ****P* < 0.001 versus the Sham + RVG-Vector-EVs group; #*P* < 0.05, ####*P* < 0.01 versus the PT + RVG-Vector-EVs group; two-way ANOVA followed by the Holm-Sidak post hoc multiple comparison test. **(D-F)** Representative Western blots showing OPA1, MFN2 and DRP1 levels in sham and

PT mice after LV-Vector or LV-KMO administration with or without RVG-circSCMH1-EVs treatment (n = 6 for each group). ***P* < 0.01, ****P* < 0.001 versus the Sham group; #*P* < 0.05, ###*P* < 0.01, ####*P* < 0.001 versus the PT + RVG-Vector-EVs group; †††*P* < 0.001 versus the PT + RVG-circSCMH1-EVs + LV-Vector group; two-way ANOVA followed by the Holm-Sidak post hoc multiple comparison test. (G) Representative confocal microscopy images of TOM20 (green, a mitochondrial outer membrane marker) in the peri-infarct cortex on day 3 after PT. DAPI, 4',6-diamidino-2-phenylindole; DRP1, dynamin related protein 1; EVs, extracellular vesicles; KMO, kynurenine 3-monooxygenase; LV, lentivirus; MFN2, mitofusin 2; OPA1, OPA1 mitochondrial dynamin like GTPase; PT, photothrombotic stroke; RVG, rabies virus glycoprotein; TOM20, translocase of outer membrane 20.

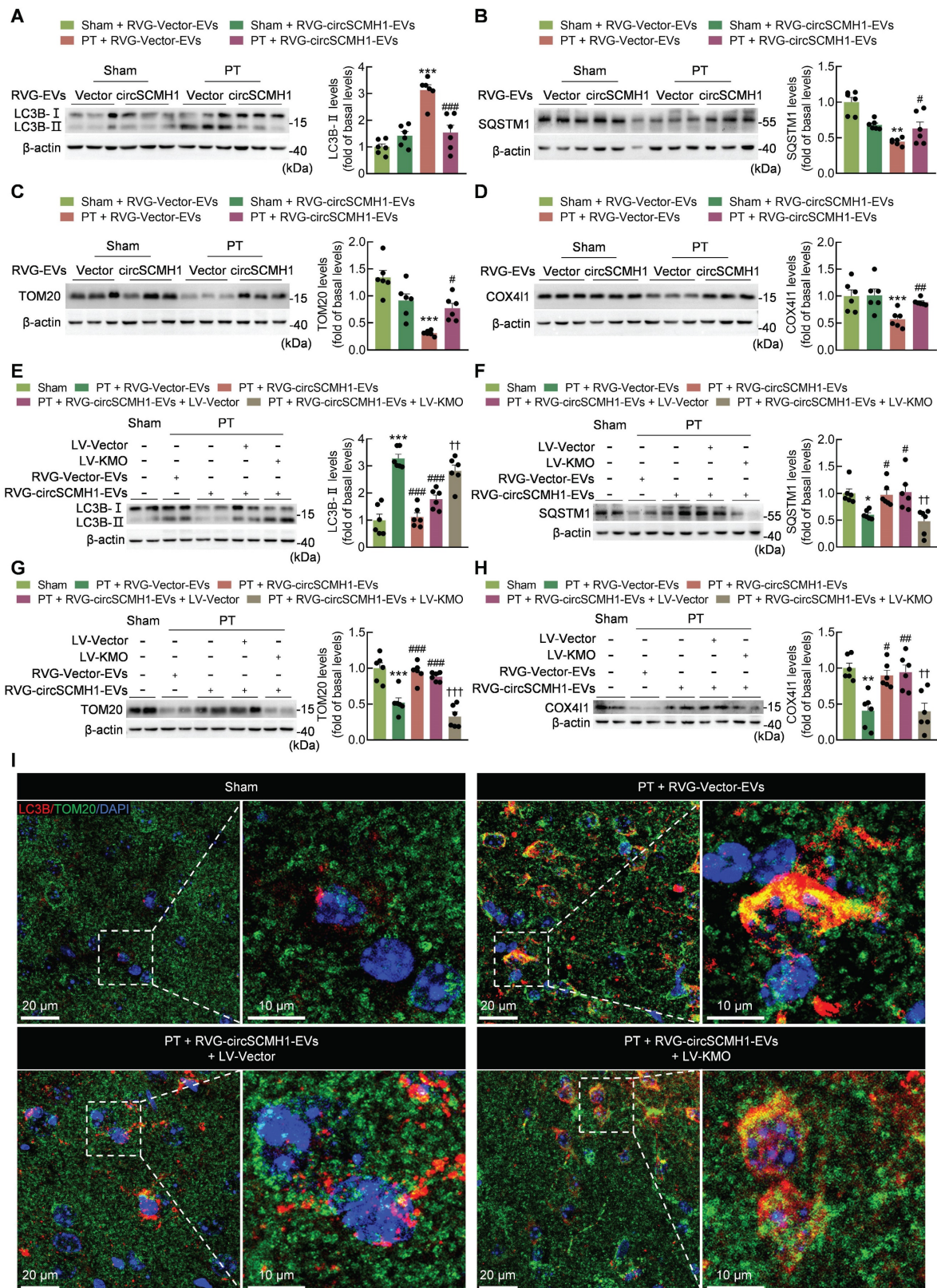


Figure 5. CircSCMH1 inhibits mitophagy via suppressing post-stroke KMO expression. (A-D) Effect of RVG-circSCMH1-EVs on LC3B, SQSTM1, TOM20, and COX411 levels in mice at day 3 after PT (n = 6 for each group). ***P* < 0.01, ****P* < 0.001 versus the Sham + RVG-Vector-EVs group; #*P* < 0.05, ###*P* < 0.01, ####*P* < 0.001 versus

the PT + RVG-Vector-EVs group using two-way ANOVA followed by the Holm-Sidak post hoc multiple comparison test. **(E-H)** Representative western blots of LC3B, SQSTM1, TOM20 and COX411 levels after LV-Vector or LV-KMO administration with or without RVG-circSCMH1-EVs treatment (n = 6 for each group). **P* < 0.05, ***P* < 0.01, ****P* < 0.001 versus the Sham group; #*P* < 0.05, ##*P* < 0.01, ###*P* < 0.001 versus the PT + RVG-Vector-EVs group; ††*P* < 0.01, †††*P* < 0.001 versus the PT + RVG-circSCMH1-EVs + LV-Vector group using two-way ANOVA followed by the Holm-Sidak post hoc multiple comparison test. **(I)** Representative confocal microscopy images of TOM20 (green, a mitochondrial outer membrane marker) and LC3B in the peri-infarct cortex at day 3 after PT. COX411, cytochrome c oxidase subunit 411; DAPI, 4',6-diamidino-2-phenylindole; EVs, extracellular vesicles; KMO, kynurenine 3-monooxygenase; LC3B, microtubule associated protein 1 light chain 3 beta; LV, lentivirus; PT, photothrombotic stroke; RVG, rabies virus glycoprotein; SQSTM1, sequestosome 1; TOM20, translocase of outer membrane 20.

Glial activation is reduced by the inhibition of KMO expression

In the brain, KMO exerts its functions in various cells and does not exhibit any clear cell type specificity [27-31]. Using markers for neurons (NeuN⁺), astrocytes (GFAP⁺ [glial fibrillary acidic protein⁺]), microglia (Iba-1⁺), and endothelial cells (CD31⁺), serial sections of the lesioned brains of PT mice were processed for immunofluorescence staining to determine the cellular distribution of KMO in the peri-infarct cortex. Neurons, astrocytes, microglia, and endothelial cells all colocalized with the KMO signal in the peri-infarct cortex (Figure S3). These results indicated that KMO had no significant cell specificity in the brain.

CircSCMH1 significantly reduces astrocytic and microglial reactivity after cerebral ischemia [18], although the mechanism is still unclear. Western blotting showed that KMO overexpression eliminated the inhibitory effect of circSCMH1 on iNOS (Figure 6A). This finding was confirmed by immunostaining, as KMO overexpression eliminated the inhibitory effect of circSCMH1 on microglial activation by increasing microglial soma size and branch number, while decreasing branch length in PT mice (Figure 6B-E). The same conclusion was drawn in astrocytes, as the overexpression of KMO promoted astrocyte activation after circSCMH1 treatment, as characterized by significantly increased GFAP levels (Figure 7A). Meanwhile, immunostaining revealed significantly increased soma size, branch number, and branch length (Figure 7B-E). These results indicated that circSCMH1 regulates mitophagy through KMO, thereby impacting glial cell activation.

Neuroplasticity and vascular remodeling are enhanced by the inhibition of KMO expression

In addition to affecting glial activation, circSCMH1 also improves neuroplasticity and vascular remodeling after ischemic stroke [18, 19]. Western blotting was used to examine the protein levels of PSD95 and synaptophysin, and the results showed that the PT mice overexpression KMO exhibited a dramatic reversal of the upregulation of the neuroplasticity markers PSD95 and synaptophysin induced by circSCMH1 treatment (Figure S4A-B). Furthermore, the fluorescence intensity of MAP2 was significantly increased in circSCMH1-treated mice and KMO overexpression

alleviated this effect (Figure S4C-D).

To investigate the potential involvement of KMO in vascular repair induced by circSCMH1 during ischemic stroke, KMO was overexpressed via lentiviral microinjection. On day 28 after PT model induction, KMO overexpression markedly reversed the elevated levels of tight junction proteins (ZO-1 and Occludin) induced by circSCMH1 treatment (Figure S5A-B). Additionally, immunostaining demonstrated that KMO overexpression significantly decreased vascular area, and total vascular length in PT mice treated with circSCMH1 (Figure S5C-E). These results indicated that KMO overexpression eliminated the beneficial effects of circSCMH1 on neuroplasticity and vascular remodeling after cerebral ischemia.

CircSCMH1 decreases *Kmo* expression and binds to STAT5B

To identify the molecular mechanisms involved in the regulation of *Kmo* expression by circSCMH1, the transcription factors predicted to regulate *Kmo* were identified using the JASPAR, AnimalTFDB and ALGGEN, databases pertaining to human and mouse transcriptional regulation. Based on the intersection of these three databases, we selected seven transcription factors that bound to the sense strand of *Kmo*. We then used the catRAPID algorithm to predict the interaction between circSCMH1 and transcription factors, revealing that STAT5B bound circSCMH1 most significantly (Table S1). In addition, ChIP experiments showed that oxygen glucose deprivation (OGD) treatment of HT-22 cells increased STAT5B binding to the *Kmo* promoter (Figure 8A-B). Meanwhile, one region of circSCMH1 (positions 426-485) exhibited a high capacity for interaction with STAT5B, and RNA pull-down assays using a biotinylated circSCMH1 probe revealed that STAT5B was pulled down at higher levels by the circSCMH1 probe as compared with the circControl probe (Figure 8C-D).

We next explored how circSCMH1 was able to regulate STAT5B as a means of affecting *Kmo* expression. Western blotting demonstrated that treatment with circSCMH1 did not alter STAT5B expression in PT mice (Figure 8E). Similarly, the total expression of STAT5B in HT-22 cells following OGD treatment did not differ significantly between circSCMH1-overexpressed and circControl groups

(Figure 8F). Notably, after OGD treatment, circSCMH1 decreased the level of STAT5B in the nucleus and increased it in the cytoplasm of HT-22 cells (Figure 8G-H). Based on these results, we concluded that circSCMH1 regulates *Kmo* expression by binding to STAT5B and inhibiting its translocation to the nucleus.

Discussion

In this study, we explored the mechanism by which KMO is involved in circSCMH1-mediated functional recovery after ischemic stroke. CircSCMH1 was found to promote functional recovery after stroke by regulating KMO expression, which was independent of KMO enzymatic activity.

Mechanistically, circSCMH1 decreased the nuclear translocation of STAT5B via direct binding to STAT5B, resulting in decreased *Kmo* expression, and thereby promoting mitochondrial fusion and inhibiting mitophagy. Finally, microglial and astrocyte activation were inhibited and neural plasticity and vascular remodeling were promoted by this circRNA, ultimately improving post-stroke repair.

Metabolic and ionic disturbances cause various forms of downstream injury after cerebral ischemia [32]. In this study, coordinated metabolomic and RNA-seq analyses were used to identify the metabolic pathways involved in ischemic stroke, revealing that the KP was regulated by circSCMH1.

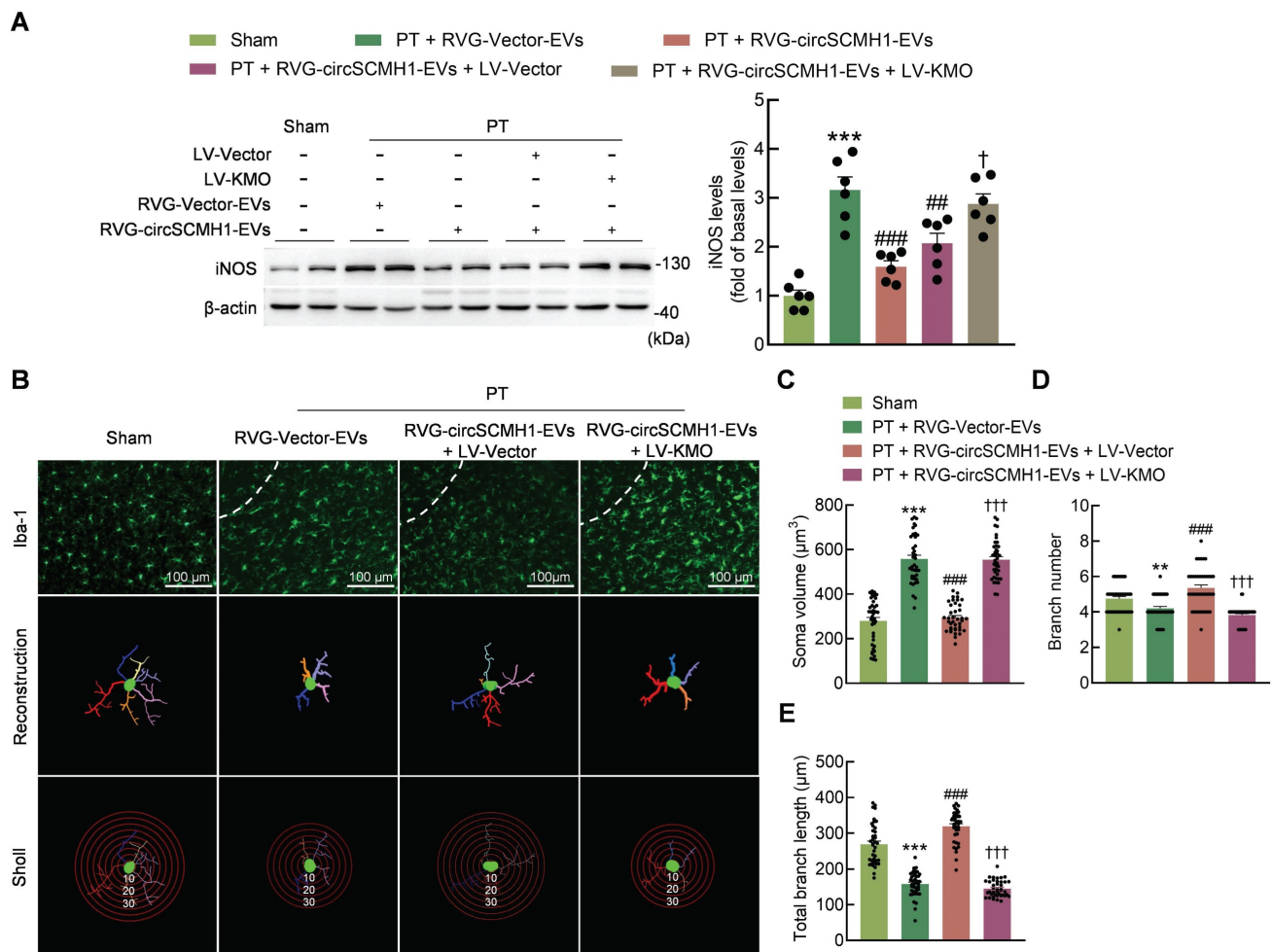


Figure 6. Microglial activation is reduced by the inhibition of KMO expression. (A) Western blotting analysis of iNOS expression after LV-KMO and RVG-circSCMH1-EVs treatment in mice at day 3 after PT. Two representative immunoblots are presented from 6 mice/group. $***P < 0.001$ versus the Sham group; $###P < 0.01$, $####P < 0.001$ versus the PT + RVG-Vector-EVs group; $†P < 0.05$ versus the PT + RVG-circSCMH1-EVs + LV-Vector group using two-way ANOVA followed by the Holm-Sidak post hoc multiple comparison test. **(B-E)** KMO abolished the inhibitory effect of RVG-circSCMH1-EVs on microglial reactivity in the peri-infarcted cortex on day 3 after PT in mice. Representative images of microglial immunostaining for Iba-1, followed by 3D reconstruction and Sholl analysis **(B)**. Average soma volume **(C)**, branch number **(D)**, total branch length **(E)** ($n = 4$ mice/group, 40 cells/group). $**P < 0.01$, $***P < 0.001$ versus the Sham group; $####P < 0.001$ versus the PT + RVG-Vector-EVs group; $†††P < 0.001$ versus the PT + RVG-circSCMH1-EVs + LV-Vector group; two-way ANOVA followed by the Holm-Sidak post hoc multiple comparison test. EVs, extracellular vesicles; iNOS, inducible nitric oxide synthase; KMO, kynurenine 3-monooxygenase; LV, lentivirus; PT, photothrombotic stroke; RVG, rabies virus glycoprotein.

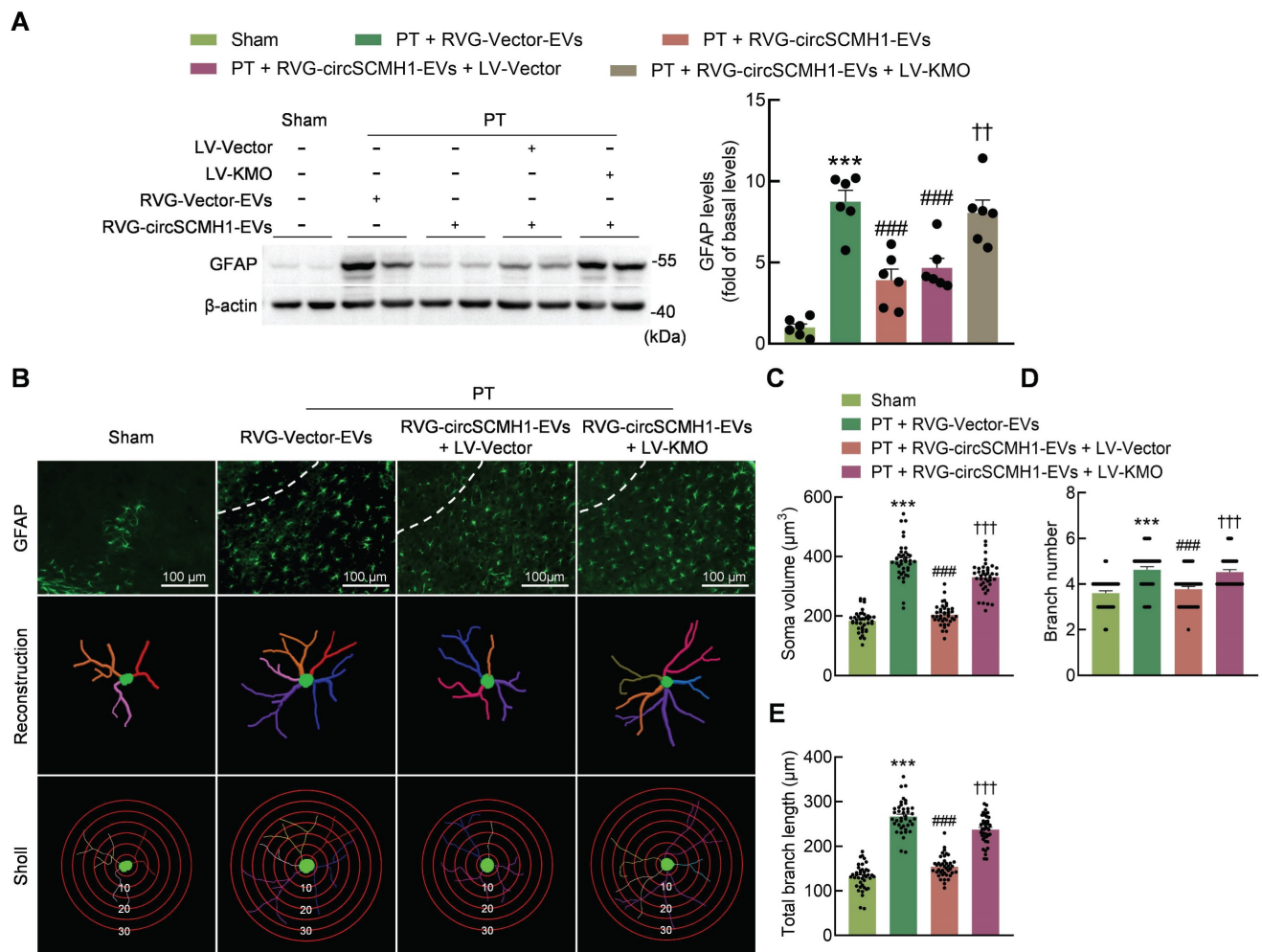


Figure 7. Astrocyte activation is reduced by the inhibition of KMO expression. (A) Western blot analysis of GFAP expression after LV-KMO and RVG-circSCMH1-EVs treatment in mice at day 3 after PT. Two representative immunoblots were presented from 6 mice/group. $***P < 0.001$ versus the Sham group; $####P < 0.001$ versus the PT + RVG-Vector-EVs group; $††P < 0.01$ versus the PT + RVG-circSCMH1-EVs + LV-Vector group using two-way ANOVA followed by the Holm-Sidak post hoc multiple comparison test. **(B-E)** KMO abolished the inhibitory effect of RVG-circSCMH1-EVs on astrocyte reactivity in the peri-infarcted cortex on day 3 after PT in mice. Representative images of astrocyte immunostaining for GFAP, followed by 3D reconstruction and Sholl analysis **(B)**. Average soma volume **(C)**, branch number **(D)**, total branch length **(E)** ($n = 4$ mice for each group, 40 cells for each group). $***P < 0.001$ versus the Sham group; $####P < 0.001$ versus the PT + RVG-Vector-EVs group; $†††P < 0.001$ versus the PT + RVG-circSCMH1-EVs + LV-Vector group using two-way ANOVA followed by the Holm-Sidak post hoc multiple comparison test. EVs, extracellular vesicles; GFAP, glial fibrillary acidic protein; KMO, kynurenine 3-monooxygenase; LV, lentivirus; PT, photothrombotic stroke; RVG, rabies virus glycoprotein.

In recent years, aberrant activation of the KP has been reported to be highly associated with ischemic stroke. Plasma levels of Trp hydroxylase and 3-HAA are downregulated in acute ischemic stroke (AIS) patients [33, 34], and an elevated serum quinolinic acid/kynurenic acid (QUIN/KYNA) ratio is a reliable biomarker of cognitive decline following stroke [35]. However, it is unclear how KP participates in the pathologic processes of ischemic stroke.

Transcriptomic analyses revealed that the level of *Kmo* was significantly increased after cerebral ischemia, and its expression was regulated by circSCMH1. Inhibition of KMO should reduce 3-HK production, and may therefore provide an efficacious approach to preventing or reducing the severity of ischemic stroke [36, 37]. However, we found that treatment with circSCMH1 did not affect the concentration of 3-HK after stroke, suggesting that the

post-stroke repair function of circSCMH1 was independent of KMO catalytic activity. KMO is a mitochondrial protein that localizes to the outer mitochondrial membrane in eukaryotic cells, and overexpression of KMO affects mitochondrial dynamics [25]. We found that the overexpression of KMO eliminated the beneficial effects of circSCMH1 on mitophagy and functional recovery after ischemic stroke. Together, our results indicated that circSCMH1 plays a role in post-stroke repair by inhibiting KMO-mediated mitophagy.

Our previous research indicates that circSCMH1 is a viable therapeutic target [18, 19]. Mitophagy regulates glial activation [38-40], which is a promising target for efforts to control cerebral ischemic injury. In the current study, the inhibitory effect of circSCMH1 on microglial and astrocyte activation was abrogated by KMO overexpression in the peri-infarct cortical

areas of mice after PT stroke. Moreover, circSCMH1 affected neuroplasticity and vascular repair after stroke through the regulation of KMO expression. Together, our results indicated that circSCMH1-mediated decreases in KMO expression inhibited glial activation following ischemic stroke.

Increasing evidence indicates that circRNAs exhibit diverse biological functions [41]. Our previous experiments have demonstrated that circSCMH1 binds to MeCP2 [18]. In addition to serving as a "miRNA sponge", circRNAs engage with

RNA-binding proteins and influence their distribution and function, as supported by recent research [42, 43]. In the present study, we found that circSCMH1 inhibited the expression of *Kmo* by binding to the transcriptional activator STAT5B [44], resulting in the inhibition of STAT5B in the nucleus and decreased expression of the downstream molecule KMO. Thus, circSCMH1 appears to have multi-target effects, suggesting that it is a promising therapeutic candidate for the treatment of ischemic stroke.

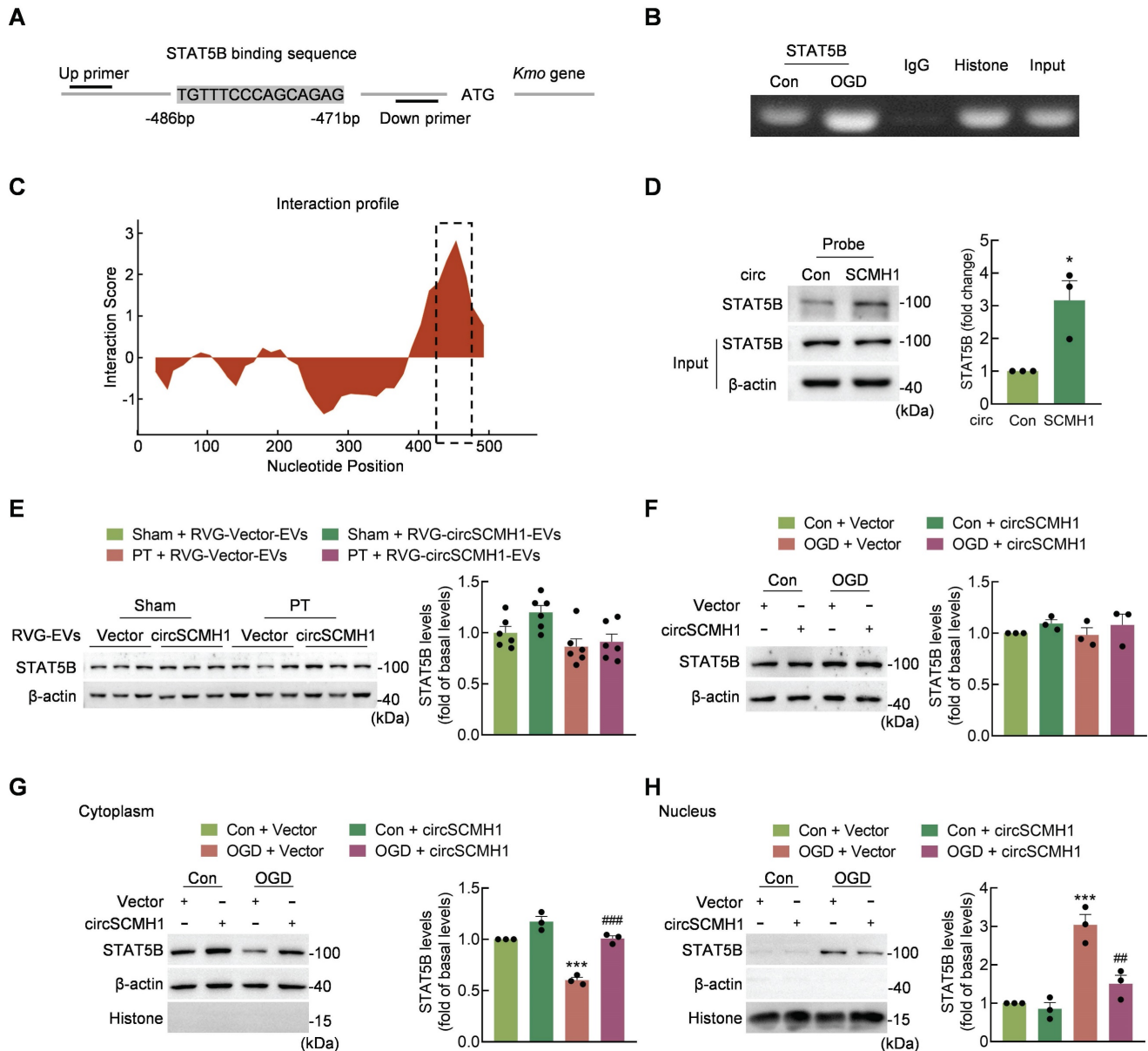


Figure 8. CircSCMH1 decreases *Kmo* expression and binds to STAT5B. (A) Illustration of the consensus binding site between STAT5B and the *Kmo* promoter. (B) ChIP assay demonstrating the ability of STAT5B to bind to *Kmo* promoter. (C) Prediction of circSCMH1-STAT5B interaction using the catPAPID algorithm. (D) Interaction between circSCMH1 and STAT5B was measured by RNA pull-down assay in HT-22 cells. All data were presented as mean \pm SEM of three independent experiments. * $P < 0.05$ versus the circControl group using Student's t-test. (E) Representative western blotting analysis of STAT5B levels after RVG-circSCMH1-EVs administration with or without PT treatment (n = 6 for each group). The significance was analyzed using two-way ANOVA followed by the Holm-Sidak post hoc multiple comparison test. (F-H) Western blotting analysis of STAT5B protein levels (F) and cytoplasmic (G) or nuclear (H) localization of STAT5B in HT-22 cells after vector or circSCMH1 plasmid transduction with or without OGD treatment for 3 h. All data are presented as means \pm SEM of three independent experiments. *** $P < 0.001$ versus the Control + Vector group; ### $P < 0.01$, #### $P < 0.001$ versus the OGD + Vector group; two-way ANOVA followed by the Holm-Sidak post hoc multiple comparison test. Con, control; EVs, extracellular vesicles; OGD, oxygen glucose deprivation; RVG, rabies virus glycoprotein; STAT5B, signal transducer and activator of transcription 5B.

Using the ALGGEN, JASPAR, and AnimalTFDB algorithms, STAT5B binding sites located within the promoter of *Kmo* were predicted. Consistent with these predictions, STAT5B was herein found to directly regulate *Kmo* expression in Chromatin immunoprecipitation (ChIP) assays. Additionally, bioinformatic prediction and pull-down assays were performed to confirm the interaction between STAT5B and circSCMH1. STAT5B is a member of the STAT protein family, members of which are transcription factors involved in various cellular processes including cell growth, differentiation, and apoptosis [45]. Previous studies have demonstrated that rats with localized cerebral ischemia and reperfusion exhibit markedly altered STAT5b levels in the hippocampus [46]. Our results suggest that STAT5B regulates the expression of KMO, with this activity in turn being regulated by circSCMH1.

The majority of global stroke guidelines now recommend intravenous thrombolysis with alteplase within 4.5 h of symptom onset [47]. Additionally, endovascular thrombectomy extends the therapeutic window for patients up to 12 h after stroke onset by rapidly reopening occluded vessels and reestablishing tissue perfusion [21]. In recent years, advancements in targeted delivery technologies and improvements in the stability and safety of nucleic acid drugs have made them a focal point in various fields of disease research. Our previous studies have shown that circSCMH1-based therapies have a relatively wider potential therapeutic window. Experimental results in non-human primate models demonstrated that RVG-circSCMH1-EVs administered 24 h after stroke significantly facilitate post-stroke brain repair, providing a more practical therapeutic window compared to existing treatments, and carrying substantial clinical implications [18]. This current study elucidated the specific mechanisms by which circSCMH1 improved functional repair after stroke by regulating mitophagy, thereby reinforcing the potential of circSCMH1 as a promising clinical therapeutic target for stroke. Our findings provide a solid theoretical foundation for advancing clinical translational research in circSCMH1.

Our study has several limitations. First, although our results demonstrating enhanced post-stroke benefits are promising, a larger sample size would increase statistical power. This expansion could potentially reveal additional significant relationships or effects undetected in our current study. Second, our study may be susceptible to potential biases arising from inherent methodological constraints. For example, the results of targeted metabolomics are particularly vulnerable to variations in sample processing procedures, which could introduce

unintended confounding factors. Third, while our results are promising, further validation in clinical settings is necessary before drawing definitive conclusions or implementing changes in clinical practice.

Taken together, the findings of this study highlight the functional link between KMO and functional recovery after stroke: The overexpression of KMO was able to promote mitophagy and aggravate post-stroke injury. circSCMH1 was found to bind to STAT5B and interfere with its nuclear translocation, leading to decreased expression of KMO, with subsequent improvements in motor functional behaviors. Our study thus provides a proof-of-concept that circSCMH1 can function as a novel inhibitor of KMO and thus has the potential to be a therapeutic target for efforts to manage metabolic disorders after cerebral ischemia.

Materials and Methods

EV isolation and purification

HEK293T (Chinese Academy of Sciences, Shanghai, China) cells were grown in 5% CO₂ in Dulbecco's modified Eagle's medium (DMEM, 10-013-CVR, Corning), supplemented with dialyzed fetal bovine serum (10% v/v, 26400044, Gibco). When the cells reached approximately 70%-80% confluence, they were co-transfected with the vector or circSCMH1-GFP plasmid and RVG-Lamp2b plasmid (71294, ADDGENE) using Lipofectamine 2000 (11668019, Invitrogen) according to the manufacturer's instructions. Forty-eight hours after transfection, hygromycin B (100 µg/ml, 108435550, Roche) and puromycin (200 ng/ml, AK058, GPC Biotechnology) were added to the cell culture medium to obtain stable strains. EVs were isolated from cell culture supernatants. Conditional medium was centrifuged at 300 × g for 5 min, 3,000 × g for 15 min, and 10,000 × g for 60 min at 4 °C to remove cells and debris. The supernatants were filtered with 0.22 µm pore filters and centrifuged at 200,000 × g for 90 min at 4 °C. Finally, the pellet was resuspended with PBS followed by another centrifugation step at 200,000 × g to purify EVs.

Animals

We conducted our tests using an all-male animal colony to eliminate the disruption of female physiological cycles and reduce the influence elements of the experiment since male and female mice differ physiologically, especially in the production of hormones. Adult male C57BL/6J mice (24.0-26.0 g, 8-10 weeks old) were purchased from the GemPharmatech (Nanjing, China) and randomly

assigned to experimental groups. All of the animals were kept in climate-controlled environments with consistent humidity and a 12-hour light/12-hour dark cycle, with the lights turned on at 7:00 AM. Food and water were available *ad libitum*. All animal experiments were approved by the Institutional Animal Care and Use Committee (IACUC) at the Medical School of Southeast University (approval ID: 20210325067) and performed in accordance with the Animal Research: Reporting of *In Vivo* Experiments (ARRIVE) guidelines. Every attempt was made to use as few animals as possible. Total 285 mice were included in this study, and 6 mice were excluded due to death ($n = 2$) or failed stroke induction ($n = 4$). Sample size required for animal study was empirically based upon the results of previous experiments and similar to that generally used in the field. Mice were coded and randomly divided into experimental and control groups.

Photothrombotic (PT) stroke mouse model

As previously described [48, 49], focal cortical ischemia was induced in mice by photothrombosis of cortical microvessels. Briefly, mice were anesthetized in a closed anesthesia chamber containing 3% isoflurane (R510-22, RWD), 30% oxygen, and 70% carbon dioxide. The rectal temperature was controlled at 37.0 ± 0.5 °C with a homeothermic blanket during surgery. Mice were treated with Rose Bengal (30 mg/kg, *i.v.*, 330000, Sigma) and then placed in a stereotaxic device. Cut the skin from the midline to expose the skull, and then cleared the surface. A cold light source (World Precision Instruments, USA) attached to an opaque template with a 2 mm diameter was positioned 1.5 mm lateral from the bregma. Five minutes after Rose Bengal administration, the brain was illuminated for 5 min, the illumination is 12,000 lux. With light excitation, singlet oxygen was generated from Rose Bengal, which damaged and occluded vascular endothelium. Sham mice received the same dose of Rose Bengal without illumination.

Intravenous delivery of circSCMH1 in animals

RVG-circSCMH1-EVs or RVG-Vector-EVs (12 mg/kg) were administered intravenously. To evaluate the effect of circSCMH1 on KMO expression and mitochondria dynamics in the PT stroke model, we divided the mice into the following groups: Sham + RVG-Vector-EVs, Sham + RVG-circSCMH1-EVs, PT + RVG-Vector-EVs, and PT + RVG-circSCMH1-EVs ($n = 6$ animals/group).

To explore the effect of KMO on functional recovery after stroke, we formed the following groups: Sham, PT + RVG-Vector-EVs, PT + RVG-circSCMH1-EVs, PT + RVG-circSCMH1-EVs +

LV-Vector, PT + RVG-circSCMH1-EVs + LV-KMO ($n = 15$ animals/group).

To confirm the function of circSCMH1 was exerted by regulating KMO expression, we formed the following groups: Sham, PT + RVG-Vector-EVs, PT + RVG-circSCMH1-EVs, PT + RVG-circSCMH1-EVs + LV-Vector, PT + RVG-circSCMH1-EVs + LV-KMO ($n = 6$ animals/group).

RNA-sequencing analysis

Whole RNA-sequencing analysis was performed by LC-Bio (Hangzhou, China). We divided the mice into the following groups: Sham + RVG-Vector-EVs, Sham + RVG-circSCMH1-EVs, PT + RVG-Vector-EVs, and PT + RVG-circSCMH1-EVs ($n = 3$ animals/group). RVG-circSCMH1-EVs or RVG-Vector-EVs (12 mg/kg) were administered intravenously 24 h after PT molding. The peri-infarct cortex from these mice were collected in TRIzol. Total RNAs were extracted from TRIzol. Each sequence fragment was given a sequence tag using UMI technology, which minimizes the interference of duplication generated by PCR amplification on the quantitative accuracy of transcriptome. Using Hisat2 (2.0.4), RNA-seq data were aligned to the mouse genome (GRCh37/hg19). Fragments per kilobase of exon per million fragments mapped (FPKM) was used to measure transcript abundance. DESeq2 was used to identify the genes that were expressed differently [50]. The Gene Expression Omnibus (GEO) accession code for the data in this manuscript is GSE261613.

Metabolomics analysis

The collected samples were thawed on ice, and metabolite were extracted with 80% methanol buffer. Briefly, 50 mg of sample was extracted with 0.5 ml of precooled 80% methanol. The extraction mixture was then stored in 30 min at -20 °C. After centrifugation at $20,000 \times g$ for 15 min, the supernatants were transferred into new tube to and vacuum dried. The samples were redissolved with 100 μ l 80% methanol and stored at -80 °C prior to the LC-MS analysis.

All samples were acquired by the LC-MS system followed machine orders. Firstly, all chromatographic separations were performed using an UltiMate 3000 UPLC System (Thermo Fisher Scientific, Bremen, Germany). An ACQUITY UPLC T3 column (100 mm \times 2.1 mm, 1.8 μ m, Waters, Milford, USA) was used for the reversed phase separation. The column oven was maintained at 35 °C. It was introduced for the separation of metabolites that the mobile phase consisted of solvent A (water, 0.1% formic acid) and solvent B (Acetonitrile, 0.1% formic acid). The gradient elution conditions were as follows with a flow rate of 0.4 ml/min: 5% solvent B for 0-0.5 min;

5-100% solvent B for 0.5-7 min; 100% solvent B for 7-8 min; 100-5% solvent B for 8-8.1 min; and 5% solvent B for 8.1-10 min. A high-resolution tandem mass spectrometer Q-Exactive (Thermo Scientific) operating in positive and negative ion modes was used to scan from m/z 70-1,000 at 70,000 resolution.

The acquired MS data pretreatments including peak picking, peak grouping, retention time correction, second peak grouping, and annotation of isotopes and adducts was performed using XCMS software. The online KEGG, HMDB database was used to annotate the metabolites by matching the exact molecular mass data (m/z) of samples with those from database. The intensity of peak data was further preprocessed by metaX. Student *t*-tests were conducted to detect differences in metabolite concentrations between 2 phenotypes ($P < 0.05$).

Liquid chromatography-tandem mass spectrometry (UHPLC-MS/MS) analysis of tryptophan metabolites

Tissues were fragmented in fivefold volume of ice-cold methanol. The samples were incubated for 20 min at -20 °C. The supernatant was collected by centrifugation, and the precipitate was extracted in duplicate. The supernatant was pooled and dried under nitrogen. Samples were redissolved with 50 μ l of 10% aqueous methanol containing 250 ng/ml of Tryptophan- $^{13}\text{C}_{11}$ internal standard. A standard mixture was newly prepared from single standard stock solution. The standard mixture was serially diluted to appropriate concentration ranges. The calibration curve sample were obtained by mixing 50 μ l of the above standard mixture with 12.5 ng tryptophan- $^{13}\text{C}_{11}$ as internal standard in insert vials, respectively. Ten-microliter volumes of each sample were injected onto a Waters ACQUITY UPLC HSS T3 Column (1.8 μ m; 100 \times 2.1 mm internal diameter, Waters, Elstree, Herts., UK) using an Agilent UPLC, coupled to an Agilent 6470 mass spectrometer. The flow rate was 0.25 ml/min. Separation was carried out using an A-water, B-acetonitrile (both containing 0.1% formic acid). The chromatographic separation was conducted by a gradient elution program as follows: 0-0.5 min, 1% B; 7 min, 60% B; 7.5 min, 99% B; 9 min, 99% B; 9.1 min, 1% B; 11 min, 1% B. The mass spectrometer was operated in positive ion electrospray mode. The Agilent MassHunter software (version B.08.00) was used to control instruments and acquire data.

Mouse behavioral tests

The mice were coded and were randomly divided into five groups. Mouse behavioral tests were performed by an independent investigator who was

blind to the experimental group.

For the grid-walking task, an elevated grid area of 32 cm \times 20 cm \times 50 cm (length \times width \times height) made of 12 mm square wire mesh was used [48, 51]. Each mouse was placed separately on the wire grid and was free to wander about until the left forelimb had taken at least 100 steps. Under the grid, a camera was placed to capture stepping errors (foot faults). In brief, it was determined to be a foot fault: 1) if a step was unable to support the foot, causing the foot to go through the grid hole; 2) if the grid was level with the mouse's wrist and it was at rest. The numbers of foot faults and non-faults for each limb were counted. A ratio was calculated as follows: number of foot faults / (number of foot faults + number of non-faults) \times 100%.

For the cylinder test [52], mice were put within a 10 cm in diameter by 15 cm height plastic cylinder, and videotaping was done for 5 min. The score was calculated as the ratio: (number of right hand – number of left hand) / (number of right hand + number of left hand + number of both hands).

For the adhesive removal somatosensory test [16, 53], 2 small pieces of adhesive-backed paper dots (of equal size, 25 mm²) were used as bilateral tactile stimuli occupying the distal-radial region on the wrist of each forelimb. Three trials per day were used to time how long it took the mice to remove each stimulus from the forelimb. Individual trials were separated by at least 5 min. Animals had three days of training prior to surgery. Once mice were able to remove the dots within 10 s, they were subjected to stroke. The result was calculated as follows (time in second): time of left hand-time of right hand.

Immunostaining and image analysis of sections

With the help of a cryostat, sections were divided into 30 μ m coronal slices. After that, they were incubated in 0.3% Triton X-100 in PBS for 15 min, followed by blocking in 10% normal goat serum (ZLI-9056, ZSGB-BIO) in 0.3% Triton X-100 for an hour at room temperature. Next, the sections were incubated with a rabbit anti-TOM20 antibody (1:100, 11802-1-AP, Proteintech), mouse anti-LC3B antibody (1:100, MA5-37852, Invitrogen), rabbit anti-Iba-1 antibody (1:200, 019-19741, Wako), mouse anti-GFAP antibody (1:200, G3893-2ML, sigma), rabbit anti-KMO antibody (1:50, 10698-1-AP, Proteintech), rabbit anti-NeuN antibody (1:200, ab104224, abcam), mouse anti-CD31 antibody (1:100, PA5-32321, Invitrogen), or mouse anti-MAP2 antibody (1:200, ab11267, abcam). On the following day, the slices were treated for an hour with Alexa Fluor 488 goat anti-mouse IgG or Alexa Fluor 488 goat anti-rabbit. After a final washing step with PBS, the sections were

mounted onto glass slides. Images were captured by microscopy (FV3000, Olympus, Japan). Three-dimensional (3D) reconstruction of Iba-1 and GFAP positive cells within the peri-infarcted cortex was performed using Computer-based cell tracing software NeuroLucida 360 (MBF Bioscience, Williston, VT, USA). NeuroExplorer (MBF Bioscience, Williston, VT, USA) was used to analyze 10 cells per mouse. Sholl analysis was used to determine branch tree morphology by placing 3D concentric circles in 5 mm increments starting at 5 mm from the soma.

RNA pull-down assays

RNA pull-down assays were performed as previously described [54]. In brief, 10^7 cells were washed in ice-cold phosphate-buffered saline and lysed in 500 μ l co-IP buffer (P0013F, Beyotime), and incubated for two hours at room temperature with 6 μ g biotin-labeled circSCMH1 probe against endogenous or ectopically expressed circSCMH1. A total of 50 μ l washed Streptavidin C1 magnetic beads (65002, Invitrogen) were added to each binding reaction and further incubated at room temperature for another hour. The beads were washed 5 times briefly with co-IP buffer. The bound proteins in the pull-down materials were analyzed by western blot. The mouse circSCMH1 probe sequence, which was biotinylated at the 5'-end, was 5'aaATTGGAGGTGTGTAGGACTTTGGTGCCAGGTGG-3'.

qPCR

qPCR was carried out using an Applied Biosystems qPCR system in accordance with our previous study. (StepOne, Thermo Fisher, USA) [18]. Total RNA was extracted using TRIzol reagent (15596026, Invitrogen). CircRNAs and mRNAs were reverse transcribed using a HiScript Q RT SuperMix for qPCR Kit (R123-01, Vazyme) and quantified using SYBR Green qPCR Master Mix (Q141-02, Vazyme). β -actin was used as an internal control. Invitrogen synthesized the primers that were utilized to amplify circRNA and mRNA transcripts. The sequences of the primers are listed in Table S2 in the Supplement.

Chromatin immunoprecipitation (ChIP) assay

The ChIP assay was conducted following the manufacturer's instructions (P2078, Beyotime). Briefly, the medium for cross-linking was immediately supplemented with new formaldehyde, and the final formaldehyde content was 1%. After 10 min of incubation at room temperature, the unreacted formaldehyde was quenched with $10 \times$ glycine for 5 min at room temperature following incubation at room temperature for 10 min. Washed cells were scraped with cold PBS containing 1 mM PMSF and

then centrifuged ($1,000 \times g$, 2 min, 4 °C) to pellet the cells. The nuclei were extracted from the cell pellet using SDS lysis buffer containing 1 mM PMSF. DNA was sheared by sonication. The fragmented, cross-linked chromatin was diluted with Protein A + G Agarose/Salmon Sperm DNA and incubated for 30 min. Following centrifugation, the cross-linked chromatin was combined with antibodies targeting STAT5B (ab178941, Abcam), Histone H3 (9715S, Cell Signaling), and IgG (2729, Cell Signaling), and allowed to incubate overnight at 4 °C. The cross-linked protein/DNA complexes were reversed to release the bound DNA using elution buffer after being cleaned with a series of cold wash buffers (including a low-salt buffer, a high-salt buffer, an LiCl buffer, and finally, a TE buffer) and purified using DNA purification spin columns. Finally, the purified DNA was amplified via PCR to identify the promoter region containing the specific binding site. The sequences of the primers are listed in Table S3 in the Supplement.

Cytoplasmic and nuclear protein extraction

Cytoplasmic and nuclear protein from HT-22 cells was prepared using the nuclear and cytoplasmic separation kit from Beyotime (P0028). Obtained supernatants were stored at -80 °C until use.

Western blot analysis

Proteins were extracted in RIPA lysis buffer (P0013B, Beyotime), separated on sodium dodecyl sulfate polyacrylamide gels (10% and 12%), and electrophoretically transferred onto polyvinylidene fluoride membranes as previously mentioned [14]. Rabbit anti-KMO antibody (1:1,000, 10698-1-AP, Proteintech), rabbit anti-OPA1 antibody (1:1,000, 27733-1-AP, Proteintech), rabbit anti-MFN2 antibody (1:1,000, 12186-1-AP, Proteintech), rabbit anti-DRP1 antibody (1:1,000, 12957-1-AP, Proteintech), rabbit anti-LC3B antibody (1:1,000, L7543, Sigma), rabbit anti-SQSTM1 antibody (1:1,000, 18420-1-AP, Proteintech), rabbit anti-COX4I1 antibody (1:1,000, 11242-1-AP, Proteintech), rabbit anti-TOM20 antibody (1:1,000, 11802-1-AP, Proteintech), rabbit anti-iNOS antibody (1:1,000, 18985-1-AP, Proteintech), mouse anti-GFAP antibody (1:1,000, 60190-1-Ig, Proteintech), mouse anti-PSD95 antibody (1:1,000, ab2723, Abcam), rabbit anti-Synaptophysin antibody (1:1,000, 17785-1-AP, Proteintech), rabbit anti-STAT5B antibody (1:1,000, ab178941, Abcam), rabbit anti-ZO-1 antibody (1:1,000, 21773-1-AP, Proteintech), rabbit anti-Occludin antibody (1:1,000, 13409-1-AP, Proteintech), rabbit anti-Histone antibody (1:1,000, 9715S, Cell signaling), or mouse anti- β -actin antibody (1:3,000, 66009-1-Ig, Proteintech) were used to detect

signals overnight at 4 °C. Membranes were then incubated with a HRP-conjugated affinity-pure goat anti-mouse or rabbit IgG(H + L) secondary antibody (1:2,000, SA00001-1 or SA00001-2, Proteintech) for an hour at room temperature. Signals were detected by chemiluminescence and imaged on a Tanon (Tanon 5200, Shanghai) digital image scanner. Quantification of individual protein bands was performed by densitometry using Image J software.

Statistics

All data are presented as mean \pm SEM. Comparisons between 2 groups were assessed with a 2-tailed Student's t-test. The homogeneity of variance was evaluated via Brown-Forsythe test. Comparisons among multiple groups (4 or more) were assessed with Two-way ANOVA followed by the Holm-Sidak post hoc test. Behavioral data collected at repeating time points (i.e., for a single animal at 5 time points) were analyzed using Two-way repeated measures ANOVA, followed by the Holm-Sidak post hoc test. The statistical analysis used for different experiments is indicated in the figure legends, and statistical significance was set at $P < 0.05$.

Abbreviations

3-HK: 3-hydroxykynurenine; ChIP: Chromatin Immunoprecipitation; COX4I1: cytochrome c oxidase subunit 4I1; circSCMH1: circular RNA SCMH1; circRNAs: circular RNAs; DAPI: 4',6-diamidino-2-phenylindole; DRP1: dynamin related protein 1; EVs: extracellular vesicles; GFAP: glial fibrillary acidic protein; GFP: green fluorescent protein; iNOS: inducible nitric oxide synthase; KMO: kynurenine 3-monooxygenase; KP: kynurenine pathway; Kyn: kynurenine; LC3B: microtubule associated protein 1 light chain 3 beta; LV: lentivirus; MAP2: microtubule associated protein 2; MFN2: mitofusin 2; OGD: oxygen glucose deprivation; OPA1: mitochondrial dynamin like GTPase OPA1; PSD95: postsynaptic density protein 95; PT: photothrombotic stroke; qPCR: quantitative polymerase chain reaction; RVG: rabies virus glycoprotein; SQSTM1: sequestosome 1; STAT5B: signal transducer and activator of transcription 5B; TOM20: translocase of outer membrane 20; Trp: tryptophan; ZO-1: tight junction protein 1.

Supplementary Material

Supplementary figures and tables 1-3.

<https://www.thno.org/v14p7292s1.pdf>

Supplementary table 4: the results of metabolomics analyses. <https://www.thno.org/v14p7292s2.xlsx>

Acknowledgments

This work was supported by the National Natural Science Foundation of Distinguished Young Scholars (82025033), the National Natural Science Foundation of China (82230115), the National Science Foundation Outstanding Youth Fund of Jiangsu Province (BK20240175), the National Natural Science Foundation of China (82473903, 82373857, 82273914, and 82304471), the Science and Technology innovation 2030-Major Project of the Ministry of Science and Technology of China (2021ZD0202904/2021ZD0202900), and the Fundamental Research Funds for the Central Universities (2242024RCB0026).

Data availability

Data that support the findings of this study are available from the corresponding author upon reasonable request.

Author contributions

Yu Wang: Writing-review & editing, Writing-original draft, Methodology, Investigation, Formal analysis. **Ying Bai:** Methodology, Funding acquisition. **Yang Cai:** Methodology, Funding acquisition. **Yuan Zhang:** Methodology, Funding acquisition. **Ling Shen:** Writing-review & editing, Methodology. **Wen Xi:** Methodology. **Zhongqiu Zhou:** Methodology. **Lian Xu:** Investigation. **Xue Liu:** Investigation. **Bing Han:** Writing-review & editing, Supervision, Funding acquisition. **Honghong Yao:** Writing-review & editing, Supervision, Methodology, Funding acquisition, Conceptualization.

Competing Interests

The authors have declared that no competing interest exists.

References

- Feigin VL, Stark BA, Johnson CO, Roth GA, Bisignano C, Abady GG, et al. Global, regional, and national burden of stroke and its risk factors, 1990–2019: a systematic analysis for the Global Burden of Disease Study 2019. *Lancet Neurol.* 2021; 20: 795–820.
- Hankey GJ. Stroke. *Lancet.* 2017; 389: 641–54.
- Murphy TH, Corbett D. Plasticity during stroke recovery: from synapse to behaviour. *Nat Rev Neurosci.* 2009; 10: 861–72.
- Moretti A, Ferrari F, Villa RF. Neuroprotection for ischaemic stroke: Current status and challenges. *Pharmacol Ther.* 2015; 146: 23–34.
- Hofmeijer J, van Putten MJ. Ischemic cerebral damage: an appraisal of synaptic failure. *Stroke.* 2012; 43: 607–15.
- Quaegebeur A, Segura I, Schmieder R, Verdegem D, Decimo I, Bifari F, et al. Deletion or Inhibition of the Oxygen Sensor PHD1 Protects against Ischemic Stroke via Reprogramming of Neuronal Metabolism. *Cell Metab.* 2016; 23: 280–91.
- Li L, Cheng SQ, Sun YQ, Yu JB, Huang XX, Dong YF, et al. Resolvin D1 reprograms energy metabolism to promote microglia to phagocytize neutrophils after ischemic stroke. *Cell Rep.* 2023; 42: 112617.
- Li Q, Wang Y, Wu S, Zhou Z, Ding X, Shi R, et al. CircACC1 Regulates Assembly and Activation of AMPK Complex under Metabolic Stress. *Cell Metab.* 2019; 30: 157–73.
- Liu X, Liu Y, Liu Z, Lin C, Meng F, Xu L, et al. CircMYH9 drives colorectal cancer growth by regulating serine metabolism and redox homeostasis in a p53-dependent manner. *Mol Cancer.* 2021; 20: 114.

10. Yu T, Wang Y, Fan Y, Fang N, Wang T, Xu T, et al. CircRNAs in cancer metabolism: a review. *J Hematonl Oncol.* 2019; 12: 90.
11. Li X, Yang L, Chen LL. The Biogenesis, Functions, and Challenges of Circular RNAs. *Mol Cell.* 2018; 71: 428-42.
12. Ashwal-Fluss R, Meyer M, Pamudurti NR, Ivanov A, Bartok O, Hanan M, et al. circRNA biogenesis competes with pre-mRNA splicing. *Mol Cell.* 2014; 56: 55-66.
13. Wilusz JE. A 360 degrees view of circular RNAs: From biogenesis to functions. *Wiley Interdiscip Rev RNA.* 2018; 9: e1478.
14. Han B, Zhang Y, Zhang Y, Bai Y, Chen X, Huang R, et al. Novel insight into circular RNA HECTD1 in astrocyte activation via autophagy by targeting MIR142-TIPARP: implications for cerebral ischemic stroke. *Autophagy.* 2018; 14: 1164-84.
15. Bai Y, Zhang Y, Han B, Yang L, Chen X, Huang R, et al. Circular RNA DLGAP4 Ameliorates Ischemic Stroke Outcomes by Targeting miR-143 to Regulate Endothelial-Mesenchymal Transition Associated with Blood-Brain Barrier Integrity. *J Neurosci.* 2018; 38: 32-50.
16. Wu F, Han B, Wu S, Yang L, Leng S, Li M, et al. Circular RNA TLK1 Aggravates Neuronal Injury and Neurological Deficits after Ischemic Stroke via miR-335-3p/TIPARP. *J Neurosci.* 2019; 39: 7369-93.
17. Chen W, Wang H, Feng J, Chen L. Overexpression of circRNA circUCK2 Attenuates Cell Apoptosis in Cerebral Ischemia-Reperfusion Injury via miR-125b-5p/GDF11 Signaling. *Mol Ther Nucleic Acids.* 2020; 22: 673-83.
18. Yang L, Han B, Zhang Z, Wang S, Bai Y, Zhang Y, et al. Extracellular Vesicle-Mediated Delivery of Circular RNA SCMH1 Promotes Functional Recovery in Rodent and Nonhuman Primate Ischemic Stroke Models. *Circulation.* 2020; 142: 556-74.
19. Li B, Xi W, Bai Y, Liu X, Zhang Y, Li L, et al. FTO-dependent m(6)A modification of Plpp3 in circSCMH1-regulated vascular repair and functional recovery following stroke. *Nat Commun.* 2023; 14: 489.
20. van Niel G, D'Angelo G, Raposo G. Shedding light on the cell biology of extracellular vesicles. *Nat Rev Mol Cell Biol.* 2018; 19: 213-28.
21. Zhang ZG, Chopp M. Exosomes in stroke pathogenesis and therapy. *J Clin Invest.* 2016; 126: 1190-7.
22. Thery C, Witwer KW, Aikawa E, Alcaraz MJ, Anderson JD, Andriantsitohaina R, et al. Minimal information for studies of extracellular vesicles 2018 (MISEV2018): a position statement of the International Society for Extracellular Vesicles and update of the MISEV2014 guidelines. *J Extracell Vesicles.* 2018; 7: 1535750.
23. Alvarez-Erviti L, Seow Y, Yin H, Betts C, Lakhil S, Wood MJ. Delivery of siRNA to the mouse brain by systemic injection of targeted exosomes. *Nat Biotechnol.* 2011; 29: 341-5.
24. Song P, Ramprasath T, Wang H, Zou MH. Abnormal kynurenine pathway of tryptophan catabolism in cardiovascular diseases. *Cell Mol Life Sci.* 2017; 74: 2899-916.
25. Maddison DC, Alfonso-Nunez M, Swaih AM, Breda C, Campesan S, Allcock N, et al. A novel role for kynurenine 3-monooxygenase in mitochondrial dynamics. *PLoS Genet.* 2020; 16: e1009129.
26. Song M, Franco A, Fleischer JA, Zhang L, Dorn GW. Abrogating Mitochondrial Dynamics in Mouse Hearts Accelerates Mitochondrial Senescence. *Cell Metab.* 2017; 26: 872-83.
27. Vecsei L, Szalardy L, Fulop F, Toldi J. Kynurenines in the CNS: recent advances and new questions. *Nat Rev Drug Discov.* 2013; 12: 64-82.
28. Schwarcz R, Bruno JP, Muchowski PJ, Wu H-Q. Kynurenines in the mammalian brain: when physiology meets pathology. *Nat Rev Neurosci.* 2012; 13: 465-77.
29. Platten M, Nollen EAA, Rohrig UF, Fallarino F, Opitz CA. Tryptophan metabolism as a common therapeutic target in cancer, neurodegeneration and beyond. *Nat Rev Drug Discov.* 2019; 18: 379-401.
30. Laumet G, Zhou W, Dantzer R, Edralin JD, Huo X, Budac DP, et al. Upregulation of neuronal kynurenine 3-monooxygenase mediates depression-like behavior in a mouse model of neuropathic pain. *Brain Behav Immun.* 2017; 66: 94-102.
31. Maganin AG, Souza GR, Fonseca MD, Lopes AH, Guimaraes RM, Dagostin A, et al. Meningeal dendritic cells drive neuropathic pain through elevation of the kynurenine metabolic pathway in mice. *J Clin Invest.* 2022; 132: e153805.
32. Daniele SG, Trummer G, Hossmann KA, Vrselja Z, Benk C, Gobses KT, et al. Brain vulnerability and viability after ischaemia. *Nat Rev Neurosci.* 2021; 22: 553-72.
33. Hajsl M, Hlavackova A, Broulikova K, Sramek M, Maly M, Dyr JE, et al. Tryptophan Metabolism, Inflammation, and Oxidative Stress in Patients with Neurovascular Disease. *Metabolites.* 2020; 10: 208.
34. Brouns R, Verkerk R, Aerts T, De Surgeloose D, Wauters A, Scharpe S, et al. The role of tryptophan catabolism along the kynurenine pathway in acute ischemic stroke. *Neurochem Res.* 2010; 35: 1315-22.
35. Cogo A, Mangin G, Maier B, Callebert J, Mazighi M, Chabriat H, et al. Increased serum QUIN/KYNA is a reliable biomarker of post-stroke cognitive decline. *Mol Neurodegener.* 2021; 16: 7.
36. Cozzi A, Carpenedo R, Moroni F. Kynurenine hydroxylase inhibitors reduce ischemic brain damage studies with (m-nitrobenzoyl)-alanine (mNBA) and 3,4-dimethoxy-[N-4-(nitrophenyl)thiazol-2-yl]-benzenesulfonamide (Ro 61-8048) in models of focal or global brain. *J Cereb Blood Flow Metab.* 1999; 19: 771-7.
37. Zwilling D, Huang SY, Sathyaikumar KV, Notarangelo FM, Guidetti P, Wu HQ, et al. Kynurenine 3-monooxygenase inhibition in blood ameliorates neurodegeneration. *Cell.* 2011; 145: 863-74.
38. Ahmed S, Kwatra M, Ranjan Panda S, Murty USN, Naidu VGM. Andrographolide suppresses NLRP3 inflammasome activation in microglia through induction of parkin-mediated mitophagy in in-vitro and in-vivo models of Parkinson disease. *Brain Behav Immun.* 2021; 91: 142-58.
39. Tang Y, Liu J, Wang Y, Yang L, Han B, Zhang Y, et al. PARP14 inhibits microglial activation via LPAR5 to promote post-stroke functional recovery. *Autophagy.* 2021; 17: 2905-22.
40. Hu ZL, Sun T, Lu M, Ding JH, Du RH, Hu G. Kir6.1/K-ATP channel on astrocytes protects against dopaminergic neurodegeneration in the MPTP mouse model of Parkinson's disease via promoting mitophagy. *Brain Behav Immun.* 2019; 81: 509-22.
41. Thomson DW, Dinger ME. Endogenous microRNA sponges: evidence and controversy. *Nat Rev Genet.* 2016; 17: 272-83.
42. Huang S, Li X, Zheng H, Si X, Li B, Wei G, et al. Loss of Super-Enhancer-Regulated circRNA Nfix Induces Cardiac Regeneration After Myocardial Infarction in Adult Mice. *Circulation.* 2019; 139: 2857-76.
43. Huang X, He M, Huang S, Lin R, Zhan M, Yang D, et al. Circular RNA circERBB2 promotes gallbladder cancer progression by regulating PA2G4-dependent rDNA transcription. *Mol Cancer.* 2019; 18: 166.
44. Klammt J, Neumann D, Gevers EF, Andrew SF, Schwartz ID, Rockstroh D, et al. Dominant-negative STAT5B mutations cause growth hormone insensitivity with short stature and mild immune dysregulation. *Nat Commun.* 2018; 9: 2105.
45. Verhoeven Y, Tilborghs S, Jacobs J, De Waele J, Quatannens D, Deben C, et al. The potential and controversy of targeting STAT family members in cancer. *Semin Cancer Biol.* 2020; 60: 41-56.
46. Sun SL, Li TJ, Yang PY, Qiu Y, Rui YC. Modulation of signal transducers and activators of transcription (STAT) factor pathways during focal cerebral ischaemia: a gene expression array study in rat hippocampus after middle cerebral artery occlusion. *Clin Exp Pharmacol Physiol.* 2007; 34: 1097-101.
47. Tsigoulis G, Katsanos AH, Sandset EC, Turc G, Nguyen TN, Bivard A, et al. Thrombolysis for acute ischaemic stroke: current status and future perspectives. *Lancet Neurol.* 2023; 22: 418-29.
48. Clarkson AN, Huang BS, Macisaac SE, Mody I, Carmichael ST. Reducing excessive GABA-mediated tonic inhibition promotes functional recovery after stroke. *Nature.* 2010; 468: 305-9.
49. Lee JK, Kim JE, Sivula M, Strittmatter SM. Nogo receptor antagonism promotes stroke recovery by enhancing axonal plasticity. *J Neurosci.* 2004; 24: 6209-17.
50. Love MI, Huber W, Anders S. Moderated estimation of fold change and dispersion for RNA-seq data with DESeq2. *Genome Biol.* 2014; 15: 550.
51. Lin YH, Dong J, Tang Y, Ni HY, Zhang Y, Su P, et al. Opening a New Time Window for Treatment of Stroke by Targeting HDAC2. *J Neurosci.* 2017; 37: 6712-28.
52. Li S, Nie EH, Yin Y, Benowitz LI, Tung S, Vinters HV, et al. GDF10 is a signal for axonal sprouting and functional recovery after stroke. *Nat Neurosci.* 2015; 18: 1737-45.
53. Hines DJ, Hayden PG. Inhibition of a SNARE-sensitive pathway in astrocytes attenuates damage following stroke. *J Neurosci.* 2013; 33: 4234-40.
54. Du WW, Yang W, Liu E, Yang Z, Dhaliwal P, Yang BB. Foxo3 circular RNA retards cell progression via forming ternary complexes with p21 and CDK2. *Nucleic Acids Res.* 2016; 44: 2846-58.